New Astronomy 101 (2023) 102022

Contents lists available at ScienceDirect

New Astronomy

journal homepage: www.elsevier.com/locate/newast

Monitoring spots via the TESS data strengthened by the ETV behaviour: An investigation on the contact binary PP Lac

M. Yılmaz [a,*], H.V. Şenavcı [a], E. Bahar [a], İ. Özavcı [a], R.H. Nelson [b,c], S.O. Selam [a], S. Zola [d], K. Gazeas [e]

[a] Ankara University, Faculty of Science, Department of Astronomy and Space Sciences, TR-06100, Tandoğan, Ankara, Türkiye
[b] 1393 Garvin Street, Prince George, BC V2M 3Z1, Canada
[c] Guest investigator, Dominion Astrophysical Observatory, Herzberg Institute of Astrophysics, National Research Council of Canada, Canada
[d] Astronomical Observatory, Jagiellonian University, ul. Orla 171, Krakow, PL-30-244, Poland
[e] Section of Astrophysics, Astronomy and Mechanics, Department of Physics, National and Kapodistrian University of Athens, Zografos, GR-15784, Athens, Greece

ARTICLE INFO

Keywords:
Stars: binaries: eclipsing
Stars: activity
Stars: individual: PP Lac
Stars: star spots

ABSTRACT

In this study we aim to reveal the starspot behaviour in the contact binary PP Lac, using the clues from the eclipse timing variation (ETV) nature of the system, obtained from the TESS data. In this context, we performed simultaneous ground-based light and radial velocity curves analysis and calculated the absolute physical and orbital parameters of the system. These parameters were then used during the light curve analysis of the TESS data for a detailed spot modelling. We considered three different spot models with: a single spot, two overlapping spots and two non-overlapping spots. The validity of each model was tested by comparing the ETV behaviour with the observed eclipse timings. The ETVs predicted by the overlapping and non-overlapping two-spot models both describe well the ETVs observed in the TESS data. In addition, the results from two-spot models indicate anti-correlated variations of spot sizes and spot longitudes throughout the TESS data time-span, whereas the longitudinal variations exhibit almost the same variation characteristics with the eclipse timings of the system. These findings imply that the longitudinal variation of spots predominantly affect the TESS-ETV behaviour of PP Lac. We conclude that the most likely explanation for light variation without eclipses and the TESS ETV behaviour in PP Lac is the presence of two high-latitude spots (or group of spots) located on the surface of the secondary component. With the help of the orbital stability tests and considering Applegate's mechanism, we found that the most plausible explanation for the two cyclic period variations seen on the overall ETV behaviour of the system is a combination of the magnetic activity cycle and the presence of a third body.

1. Introduction

Analysis of the data from space based missions is crucial, especially to reveal the nature of long term variations on i.e. pulsating stars or magnetically active stars. The high quality space mission data also enabled the identification of random walk-like variations or quasi-periodicities in the eclipse timing variations of contact binary systems, which can be explained by the presence of starspots (Tran et al., 2013). Motivated by studying eclipsing binary stars more accurately in the era of space-borne data, we carried out a detailed orbital analysis of the contact binary PP Lac using the radial velocity data of the system obtained for the first time as well as the ground-based multi-colour photometry that are analysed simultaneously. Based on the derived system parameters, we also investigated the TESS data of the system in terms of light curves and the eclipse timings, in order to reveal signs of a long-term activity. In addition, we studied the overall eclipse timing variation of the system using the most recent timings available in the literature, as well as eclipse timings obtained in this study.

PP Lac (TIC66080183, $m_v = 11\overset{m}{.}85$, $m_G = 11\overset{m}{.}67$) was discovered by Miller and Wachmann (1971), after collecting and examining the photographic data covering $\sim$ 20 years and classified the system as RR Lyr or EW type binary with a period of about 0.5 days. Figer and Rolland (1977) re-classified the system as EW type system with an orbital period of 0.4011 days, based on data from a 25 cm reflecting telescope. The first B and V band photoelectric light curves of the binary

* Corresponding author.
E-mail address: mesutyilmaz@ankara.edu.tr (M. Yılmaz).

https://doi.org/10.1016/j.newast.2023.102022
Received 31 October 2022; Received in revised form 8 February 2023; Accepted 23 February 2023
Available online 26 February 2023
1384-1076/© 2023 Elsevier B.V. All rights reserved.

were obtained by Dumont and Maraziti (1990). Gaspani (1990) performed the first orbital solution of the system using the data gathered by Dumont and Maraziti (1990). They determined the mass ratio of the system as 0.6 and pointed out that the components of the system have nearly equal effective temperatures. Al-Naimiy and Al-Hindawy (1992) performed a Fourier analysis on the same data and confirmed that the system is a typical W UMa type binary and determined its mass ratio to be 0.32. They also found the orbital inclination and the temperature ratio of the system as 80° and 0.95, respectively. Sanders et al. (2004) gathered light curves of the system in V and Rc bands, revealing the total primary eclipse. The authors noted that their mass ratio to be well-constrained by the duration of the total eclipse and also mentioned PP Lac was a W-type contact binary. Sanders et al. (2004) also performed a period analysis of the system covering 30000 cycles and found a period decrease of -1.082×10^{-2} s yr^{-1}. The V-band CCD photometric study of PP Lac was carried out by Qian et al. (2005), who confirmed the system to be a W-type W UMa binary with the mass ratio $q = M_2/M_1 = 2.3$ via the photometric q-search. They found the temperature difference between components to be 260 K. Using nearly the same time span of available minima times, Qian et al. (2005) carried out another period analysis and found a cyclic variation with a period and amplitude of 19.7 years and 0.0058 days, respectively. The most recent photometric study of the system was performed by Kjurkchieva et al. (2020), who observed the system in SDSS g' and i' bands. They calculated the effective temperature of the primary component to be 6050 K, by taking the average of the effective temperatures from GAIA DR2 (Gaia Collaboration et al., 2018), 2MASS (J-K) and (g' - i') colour indices, also considering dereddening. From the light curve analysis, they obtained $q = 2.555$, $i = 84°.7$, and $T_2 = 5678$ K. They mentioned the light level difference between the two quadratures, second quadrature being fainter than the first one, and attributed it to the presence of cool spot(s). For this reason, in their solution, they placed a cool spot at 90° co-latitude and 90° longitude with a temperature factor of 0.87 and a diameter of 28°, on the more massive secondary component. With the help of the period analysis covering almost 38000 cycles, they obtained a cyclic variation with an amplitude of 0.005 days and a period of 23 years. They also mentioned the presence of "stepped" sections seen in the last 12000 cycles with duration of 2–3 years and essentially constant period.

2. Observations and data reduction

2.1. Ground-based observations and data reduction

The spectroscopic data of PP Lac were gathered between August 27–September 10, 2020 at the Dominion Astrophysical Observatory (DAO), using the Cassegrain spectrograph attached to the 1.85 m Plaskett telescope. A total of 11 spectra were obtained covering a wavelength range from 5000 Å to 5260 Å, with a resolving power of R ≈ 10,000. The reduction procedure, such as bias and flat corrections, removal of cosmic rays, extraction of orders, wavelength calibration and continuum normalization were performed with the help of the RaVeRe[1] software. The radial velocity measurements of the system were carried out using the Broad[1] software that is based on the broadening functions (BF) routine (Rucinski, 2004). The standard Fe I lines at 5041.755, 5167.487, 5171.585, 5227.15 Å were used during the determination of radial velocities. The radial velocity curve of the system is shown in the right panel of Fig. 4.

The ground-based photometric CCD observations of the system were carried out with the 0.8 m Prof. Dr. Berahitdin Albayrak Telescope (hereafter T80 Telescope) at the Ankara University Kreiken Observatory (AUKR), during October 16, 2020. The multi-colour photometric data of PP Lac were gathered using the Apogee Alta U47 CCD camera and the SDSS g', r' and i' filters that are attached to one of the Nasmyth foci of T80 Telescope. All raw images were reduced in the usual manner by using bias, dark, and sky-flat images with the help of the `AstroImageJ` software (Collins et al., 2017). We made use of the same software during the differential photometry procedure, in which differential magnitudes were computed in the sense variable minus comparison (TYC 3984-1063-1), whose variability was checked against the check star (TYC 3984-1081-1). A total of 367, 372 and 356 points were obtained with the average errors of 0.003 mag, 0.002 mag and 0.002 mag for g', r' and i' filters, respectively.

Both the light and the radial velocity data were phased using the ephemeris (light elements) given in Eq. (1) below, which is calculated from the ground-based photometric observations performed in this study. The light curves of the system are illustrated in the left panel of Fig. 4.

$$HJD_{\mathrm{MinI}} = 2459139.44226(4) + 0^{\mathrm{d}}.40116493(6) \times E. \quad (1)$$

2.2. TESS light curves

We collected the TESS data of PP Lac from the MAST Portal.[2] The system was observed in sectors 16 and 17 of the TESS observations that comprise the dates September 12–October 06 and October 08–November 02, 2019, respectively. Sector 16 covers a period of 23.38 days and the data collection was paused for 1.29 days while downloading data during perigee passage. In Sector 17, the data collection time span was 23.51 days, while the pause was 1.43 days. During the preparation of the data for the light curve analysis, we first compared SAP and PDCSAP data, in order to check if there are any long-term astrophysical trends that could have been removed due to the automated pipeline process. We found out that there is a significant amplitude difference between SAP and PDCSAP light curve data, where PDCSAP data have relatively higher amplitude.

The SAP data of sectors 16 and 17 also have different amplitudes due to the slightly different photometric apertures (pixel masks) for both sectors specified by SPOC pipeline (see the upper panel of Fig. 1 - grey shaded area) and hence the different amounts of light/background contamination along with the crowded region. Such amplitude differences may prevent the precise determination of the system and/or spot parameters. Therefore, we re-did photometry of sectors 16 and 17, with several different pixel masks created using the threshold parameter in the `Lightkurve` package (Lightkurve Collaboration et al., 2018) and by cutting out the background stars with the help of the cut-out function (Brasseur et al., 2019). However, we obtained the coherent light curve amplitudes of the two sectors using manually selected pixels that is shown at the upper panel of Fig. 1.

It is also clear from the upper panel of Fig. 1 that the apertures specified by SPOC pipeline (grey shaded area) include two more objects (S2[3] and S3[3] in Fig. 1) with Gaia magnitudes of 14.4 and 15.8. On the other hand, the selected pixels during re-photometry process do not include S3 and therefore the effect of S3 in the resultant light curves was removed. The details on how we considered the light contribution of S2 were given in detail, in Section 4. In the next step, we stitched the sectors 16 and 17, by matching the average flux of the last two cycles of sector 16 to the first two cycles of sector 17, based on the method by Revalski et al. (2014) and Kasliwal et al. (2015). All the flagged data points were removed in order to eliminate any flux anomalies affected by non-nominal operating conditions on the spacecraft as described in Tenenbaum & Jenkins.[4] Consequently, we selected 96 cycles of PP Lac for the analyses.

[1] http://binaries.boulder.swri.edu/binaries/software/

[2] https://mast.stsci.edu/portal/Mashup/Clients/Mast/Portal.html

[3] Gaia DR2 catalogue names of S2 and S3 objects are 2002302453348955392 and 2002302449044616064, respectively

[4] Tenenbaum, P., & Jenkins, J. M. 2018, TESS Science Data Products Description Document EXP-TESS-ARC-ICD-0014 Rev D

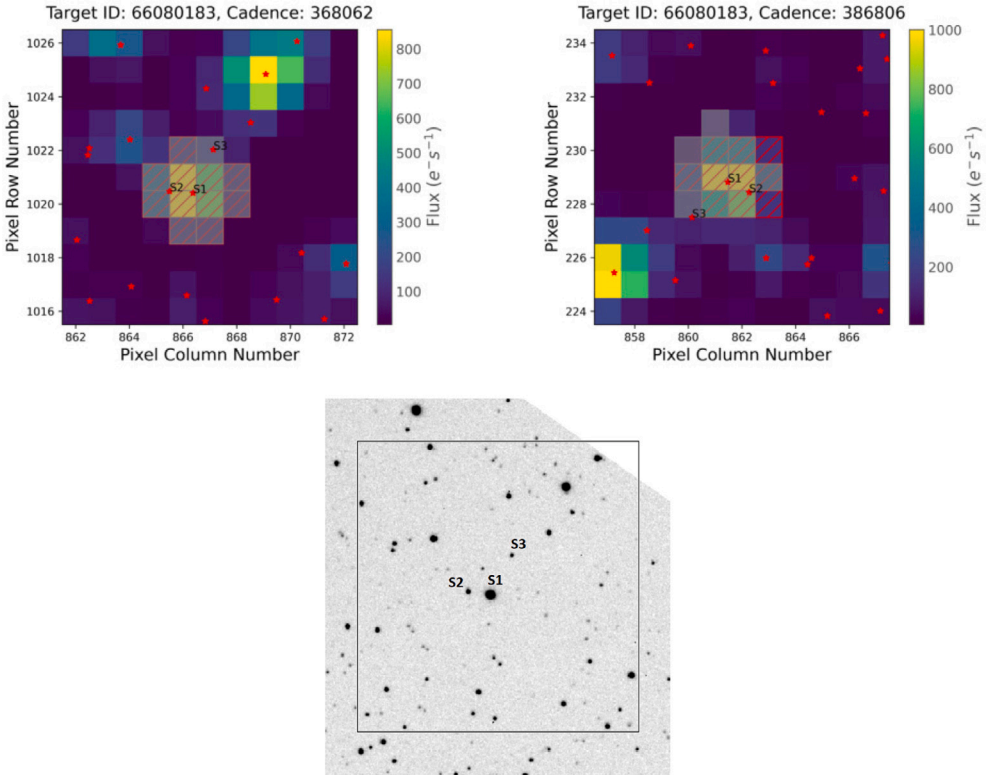


Fig. 1. Upper panel: Examples of CCD frames for Sectors 16 (left) and 17 (right). The masks used by the SPOC pipeline and simple aperture photometry that is performed in this study are shown with grey shaded and red hatched regions, respectively. S1 denotes PP Lac, while S2 and S3 stands for closest neighbouring stars that are inside the SPOC-mask. Lower panel: An example of a CCD frame from ground-based observations, which has been cropped for comparison with the TESS FoV. Note that the Sector 16 and ground-based image have roughly the same orientation, whereas the Sector 17 image is rotated by ∼160° counter-clockwise.

Although the TESS data includes light contamination due to the huge pixel scale (21*21 arcsecs) of CCD and the crowded region of PP Lac as shown in Fig. 1, such time-series and almost continuous data provides an unprecedented opportunity not only to reveal the existence of spots but also to trace the variation of some spot parameters (i.e. spot longitude). In addition, the light curves obtained by Kjurkchieva et al. (2020) and this study (see Fig. 4), in which flux at the phase 0.75 is fainter than at 0.25, clearly shows the O'Connell effect that can be attributed to the presence of cool spot(s) on one or both components of the system. Therefore, we consider the TESS data of the system only for spot modelling, of which the details are given in Section 4. In this context, we investigated the flux level of each orbital cycle during non-eclipsing phases 0.25 (Max I) and 0.75 (Max II), by fitting polynomials within $\Delta\phi = \pm 0.05$ intervals and plotted them in Fig. 2. The variation of maxima flux levels with an average error of 0.0019 in units of normalized flux throughout the entire data is clearly visible. The displacement of Max I and Max II levels in the middle of sector 17 is another noticeable feature. We also checked that there is no difference between the flux level variations of the data that we derived via re-photometry and PDCSAP data. We also plotted the flux differences of quadrature phases in the lower panel of Fig. 2, where the cyclic oscillations exist similar to that is seen in EE Cet, studied by Yang and Wang (2023).

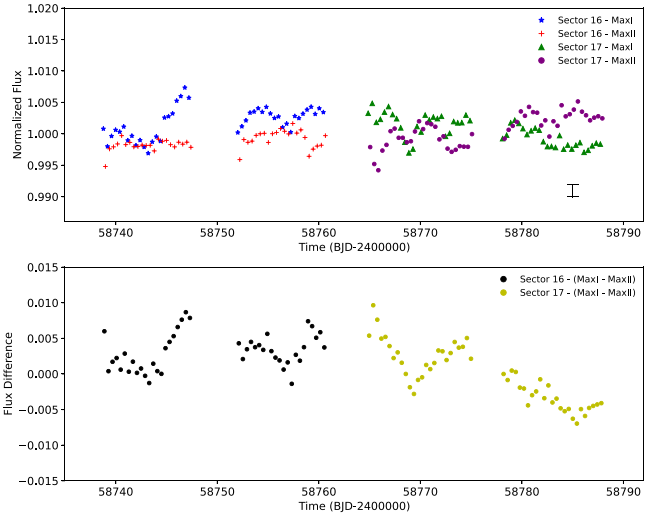


Fig. 2. Maximum flux level variations (upper panel) and their differences (lower panel) obtained using the TESS data of PP Lac for sectors 16 and 17. The error bar located at the bottom of the upper panel represents the average error.

2.3. Eclipse timing variations of the TESS data

We also investigate the eclipse timing variations (ETV) of the TESS data, in order to search for any traceable short time-scale variations in the ETV diagram. In this context, we used a Python-based GUI software, `Xtrema` (Bahar et al., 2015), to calculate the primary and secondary eclipse timings. We derived 43 primary and 44 secondary eclipse timings for Sector 16, 52 primary and also 52 secondary eclipse timings for sector 17, that correspond to 191 eclipse timings in total. All obtained TESS minima times can be found in the CDS linked to this study. The ETV diagram of PP Lac including only the TESS data of the system is generated using the following light elements (Eq. (2)), which is updated from the ephemeris of ground-based observations and is plotted in Fig. 3.

$$BJD_{\mathrm{MinI}} = 2459139.44056(2) + 0^{\mathrm{d}}.40116107(3) \times E. \quad (2)$$

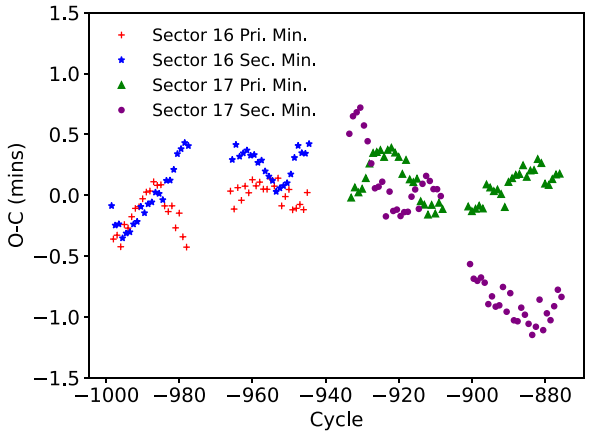


Fig. 3. ETV diagram of PP Lac generated using the TESS data. Red plus and blue asterisk signs represent the primary and the secondary eclipse timings of Sector 16, respectively, while purple filled circles and green triangles show the same for Sector 17.

The ETV diagram of PP Lac generated using only the TESS data of the system clearly shows random walk-like or quasi-periodic variations, as well as an anti-correlated behaviour between the variations of the primary and secondary eclipse timings. The anti-correlation is much more apparent in Sector 17, while Sector 16 shows both positive and negative correlations. Similar behaviour was studied in detail by Tran et al. (2013), who explained it by the presence of a starspot that is continuously visible around the orbit and slowly changes its longitude on timescales of weeks to months. Another remarkable point is the presence of the same anti-correlation in the variation of maxima flux levels, as seen in Fig. 2. Therefore, those variations observed in both the period and the light curves can be considered as important evidence for the presence of spot(s) in PP Lac. We discuss the underlying cause of the ETV nature of PP Lac in Section 5.

3. Ground-based light and radial velocity curve analysis

We simultaneously analysed the light and radial velocity curves of the contact binary PP Lac using the PyWD2015 code (Güzel and Özdarcan, 2020) developed in Python, which is a graphical user interface (GUI) that is based on the 2015 version of the Wilson–Devinney (WD) code (Wilson and Devinney, 1971). We assumed the system as an over-contact binary and therefore selected Mode-3 in PyWD2015. During the analysis, the effective temperature of the primary component was fixed to T_1=6050 K, the value given by Kjurkchieva et al. (2020). The gravity darkening and the albedo coefficients were set to 0.32 (Lucy, 1967) and 0.5 (Ruciński, 1969), respectively, which are appropriate values for the spectral types of both components. The limb darkening coefficients were interpolated automatically from the van Hamme (1993) tables under the linear-cosine law assumption. We adjusted the effective temperature of the secondary component (T_2), common surface potential of components ($\Omega_1 = \Omega_2$), orbital inclination (i), the monochromatic luminosity of the primary component (L_1), the system mass ratio (q), semi-major axis (a), and the gamma velocity (V_γ) during the simultaneous analysis. During the trials, we also adjusted the third light parameter (l_3 - third light in flux unit) but could not get convergence.

The flux modulation of TESS data along with the orbital phase, the unequal maxima levels of the ground-based light curves as well as the preliminary simultaneous LC+RV data analysis results showed that reliable system parameters can only be obtained by considering hot or cool spot included in the model. As mentioned in Section 1, the same approach was recently applied by Kjurkchieva et al. (2020), who assumed one cool spot with a radius of 28 degrees that is located on the equator of the more massive secondary component in their light curve analysis. On the other hand, in the case of such rapid rotators, the spots are expected to occur at high latitudes and polar regions, which is mentioned by Schuessler and Solanki (1992). In addition, contact or near contact binaries having high latitude or polar spots are well-known in the literature, of which their surface inhomogeneities were investigated via Doppler imaging technique (i.e., Hendry and Mochnacki, 2000; Barnes et al., 2004; Xiang et al., 2015). Therefore, we started the simultaneous analysis by assuming a high latitude spot located on the more massive secondary component. We derived the relative spot temperature as T_{sp}=0.7, using the equation that is based on the ratio of starspot temperature to stellar effective temperature given by Maehara et al. (2017) and kept it fixed during the analysis, while the longitude, co-latitude and the radius of the spot along with the other system parameters mentioned above were adjusted. The observed light and radial velocity curves together with their models and residuals are plotted in Fig. 4, while the system geometry of PP Lac as well as the spot distribution at phases 0.00, 0.25, 0.50 and 0.75 are illustrated in Fig. 5. The parameters obtained from the simultaneous multi-colour light and radial velocity curve modelling as well as the absolute parameters are summarized in Table 1. It should be noted that

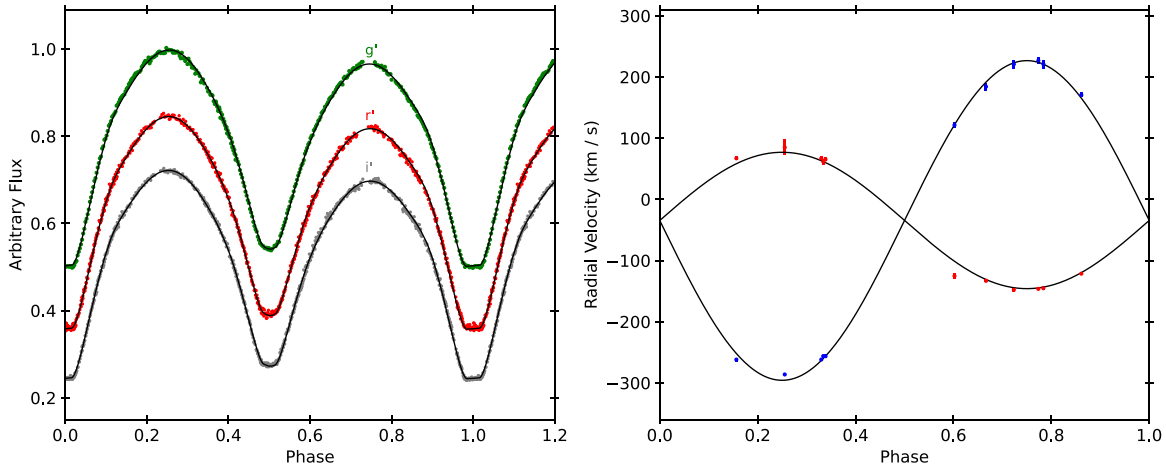


Fig. 4. Ground-based g', r', i' light curves (left panel) as well as the radial velocity curve (right panel) of PP Lac and the best model fits (black solid lines) using Mode-3 of W-D.

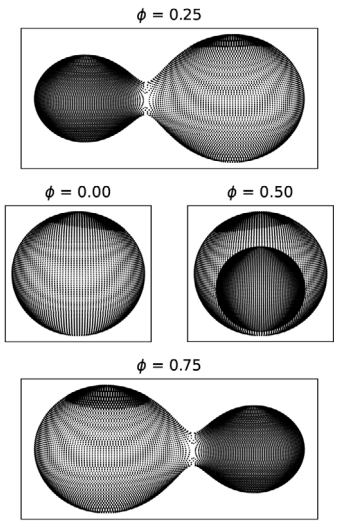


Fig. 5. System geometry of PP Lac for phases 0.00, 0.25, 0.50 and 0.75 that is obtained from the ground-based data analysis.

the formal errors provided by the WD code are underestimated, since they are based on a quadratic approximation for the dependence of χ^2 on the model parameters in the region of the best fit (Maxted et al., 2020).

From the simultaneous analysis of the system photometric and spectroscopic observations, we obtained the spot co-latitude as $\varphi = 7°.78 \pm 0.12$ (corresponding to the latitude value of 82°.22), the longitude as $\lambda = 272°.66 \pm 0.88$ and the radius as $\theta = 37°.73 \pm 0.07$. These correspond to the presence of a polar (or a high-latitude) spot that is best visible at phase 0.75, which is also clear from the light curves of the system shown in the left panel of Fig. 4.

4. Spot modelling using TESS light curves

Reliable monitoring of spots using long-term light curve data requires a consistent set of orbital and geometric parameters, implying that only the spot parameters may cause the intrinsic light curve variation. The simultaneous ground-based light and radial velocity curve analysis performed in this study has enabled us to determine reliable system parameters of PP Lac. In this context, we examined cycle to cycle variation of the TESS light curves and hence analysed each cycle individually, using the system parameters obtained from ground based data. The aperture masks used for the reprocessed TESS photometry include S2, as mentioned in Section 2.2. Thanks to the ground-based observations that we were able to resolve S2 individually, we calculated the light contribution in terms of flux as $l_3 = 7.7\%$ in the i' band. It should be noted specifically for such systems with high orbital inclination and having a high latitude or a polar spot that l_3 and spot radius parameters degenerate each other; as the amount of l_3 increases, the radius of the spot becomes larger.

We took the first cycle of TESS Sector 16 (cycle −999) as the reference light curve and assumed one high latitude cool spot on the secondary component. We used the spot parameters obtained from ground-based solution as preliminary parameters and adjusted spot co-latitude, radius and longitude, while the spot temperature was fixed to *Tsp*=0.7. We also adjusted L_1, in order to obtain the TESS passband luminosities. For the spot modelling of the rest of the cycles, we follow the strategy whereby the spot parameters obtained from the previous cycle were used as the input spot parameters of the next cycle. The TESS limb darkening coefficients were taken from the 2019 update of WD2015[5] and adopted to PyWD2015. Therefore, we were able to interpolate the LD coefficients automatically from the updated LD tables under the linear-cosine law approximation. The rest of the system parameters including l_3 were fixed. It should be noted that during the analysis of the TESS light curves, the l_3 value obtained from the i' band was used since the i' band and TESS filter have almost similar central wavelengths. For the single spot model, the observed and synthetic light curves with their residuals for selected cycles are plotted in Fig. 6. Variation of spot longitudes, co-latitudes and radii along with the cycle were also plotted in Fig. 7.

[5] https://faculty.fiu.edu/~vanhamme/lcdc2015/

Table 1
Results from the light curve analysis using the ground-based data (with formal errors from the WD code) and the absolute parameters of PP Lac. Final sum of squares of residuals between observed and synthetic light curves ($\sum(O-C)^2$) for g', r' and i' bands are calculated as 0.0078, 0.0048 and 0.0028, respectively.

Parameter	Value	Parameter	Value
i [°]	83.9 ± 0.8	λ [°]	272.7 ± 0.9
$a[R_\odot]$	2.971 ± 0.021	θ [°]	37.7 ± 0.1
V_γ [km/s]	-34.49 ± 1.41	Tsp	0.7
$q = M_2/M_1$	2.344 ± 0.002	M_1 $[M_\odot]$	0.66 ± 0.01
T_1 [K]	6050	M_2 $[M_\odot]$	1.54 ± 0.03
T_2 [K]	5740 ± 3	R_1 $[R_\odot]$	0.96 ± 0.01
$\Omega_{1,2}$	5.576 ± 0.003	R_2 $[R_\odot]$	1.40 ± 0.02
$L_1/(L_T)$ $[g']$	0.375 ± 0.005	L_1 $[L_\odot]$	1.11 ± 0.02
$L_1/(L_T)$ $[r']$	0.368 ± 0.004	L_2 $[L_\odot]$	1.90 ± 0.11
$L_1/(L_T)$ $[i']$	0.360 ± 0.003	log g_1 [cgs]	4.29 ± 0.01
φ [°]	7.8 ± 0.1	log g_2 [cgs]	4.33 ± 0.01

Although the overall fits look convincing as seen in Fig. 6, solutions for some cycles resulted in unsatisfactory description of observations by model light curves, as they failed to model maxima levels, minima depths and especially the asymmetries around maxima profiles (i.e. cycle −955, the top right panel of Fig. 6). The average spot radius was obtained as 53° (see Fig. 7), which is somewhat larger than that obtained from ground-based observations. This may be a consequence of an increase in the spot radius over a time span of ∼ 1 year between TESS and ground-based observations or an indication of the degeneracy between l_3 and spot parameters, as a polar spot dims the overall lightcurve, while additional light brightens. Fixing the spot radius to the value that we obtained during the ground-based solution gave the l_3 value of 0.042. However, assuming that the l_3 value determined from ground-based data is reliable, we kept its value fixed as 0.077 during the analysis. Another remarkable point is the longitudinal variation of spot along with the orbital cycle, as seen from the left panel of Fig. 7. A very rapid longitudinal migration of the spot is evident between the cycles −925 and −909 that corresponds to a rate of ∼17° cyc^{-1}, while the rest of the longitudinal drift is about ∼ 1.4° cyc^{-1} (3.54° day^{-1}). The mid and right panels of Fig. 7 show the variations of spot size and latitude, where there are no significant change.

As a second trial, we introduced two spots located on the secondary component, as the one-spot modelling was particularly inadequate to especially represent both maximum variations as well as the asymmetries in some cycles. In this context, the second spot has the same parameters as the first spot, except the longitude that is centred 180° opposite to the first one. We then adjusted spot longitude, co-latitude and radius parameters of both spots for the LC modelling of our reference cycle (cycle -999). The co-latitude values were obtained as $9°.7 \pm 0.1$ and $9°.8 \pm 0.1$, resulting in two spots overlapping each other by ∼83%. This causes the temperature factor of the overlapping region to be ∼0.5, since the overlapping spot temperature is obtained by the product of the individual spot temperature factors. In order to keep the spot temperature as 0.7, which is obtained using the equation given by Maehara et al. (2017), we fixed *Tsp* as 0.83. Consequently, during the LC analyses of the entire data under two-spot model, we adjusted the spot longitudes and radii, while we fixed the co-latitude and *Tsp* parameters to those obtained from the LC modelling of our reference cycle.

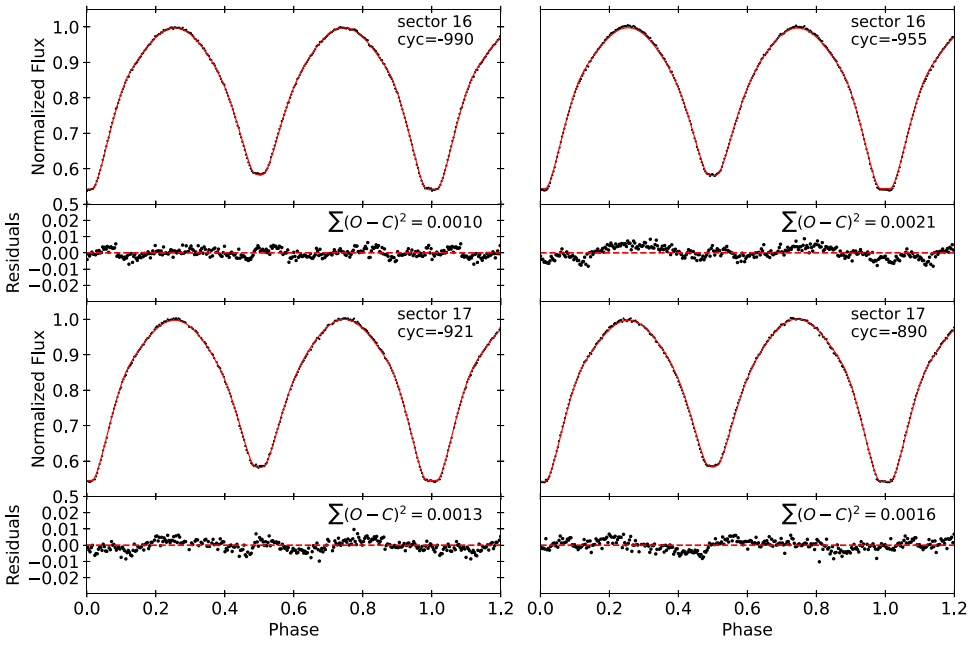


Fig. 6. A sample of TESS light curves as well as their best model fits (red solid lines) of PP Lac under single spot approximation. Residuals from the theoretical fits are indicated at the bottom of each curve. Note that the cycles are calculated using Eq. (1).

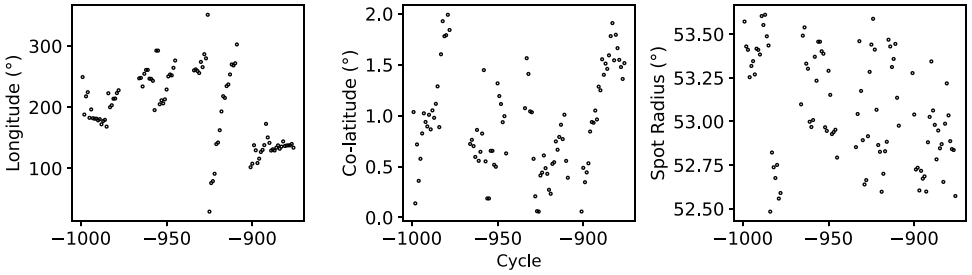


Fig. 7. Cycle to cycle variation of spot longitude, co-latitude and radius obtained for a single spot approximation.

The observed and synthetic light curves of the two-spot model, with their residuals for selected cycles are plotted in Fig. 8. Variation of spot longitudes and radii along with the cycle were also plotted in Fig. 9. Compared to single spot modelling, we obtained better model fits via two-spot model, as we obtained lower $\Sigma(O-C)^2$ values (see Fig. 8). From the top panel of Fig. 9, it is clear that both spots exhibit similar behaviour in terms of longitudinal variation with a migration towards decreasing longitudes and then higher longitudes with almost the same drift rates. On the other hand, as seen from the bottom panel of Fig. 9, the variation of the spot radii evidently shows an anti-correlation with an average amplitude of ∼4°.

In addition to the overlapping two-spots modelling, we searched for a possible non-overlapping two-spot configuration. Assuming the spot temperature fixed at *Tsp*=0.7, our attempts converged to such a configuration, where two spots are located at $28°.0 \pm 0.3$ and $25°.1 \pm 0.2$ co-latitudes with the spot radii of $25°.6 \pm 0.1$ and $27°.2 \pm 0.1$, and the longitudinal separation of ∼173°5. The best fit models with their residuals for selected cycles are plotted in Fig. 10, while the variation of spot longitudes and radii along with the cycle were illustrated in Fig. 11.

The resultant fits for non-overlapping two-spot model gave higher $\Sigma(O-C)^2$ values than the overlapping two-spot model, as can be clearly distinguished from Fig. 10. On the other hand, residuals of non-overlapping two-spot model are still less scattered than the single spot model. Comparing the longitude-radius variations of both two-spots approximations (Figs. 9 and 11), it is seen that the behaviour is similar, while both the variation amplitudes of spot longitudes and radii in the non-overlapping two-spot model are lower. As a result, depending on the $\Sigma(O-C)^2$ values, it can be interpreted that among three different spot scenarios considered for PP Lac system using the TESS data, the overlapping two-spot model is the one that best fits the entire light curves. The $\Sigma(O-C)^2$ values for the light curve analyses of three spot models are summarized in Table 2. It should be noted that neither of the spots in three spot models are occulted during the entire orbital cycle.

Table 2
$\Sigma(O-C)^2$ values for three spot models.

Model	$\Sigma(O-C)^2$
Single spot	0.00234
Overlapping two-spot	0.00128
Non-overlapping two-spot	0.00130

5. Testing the spot models with ETV

As mentioned in Section 1, the ETV nature of PP Lac obtained using the TESS data should be caused most likely by the presence of spots. Therefore, we expect the eclipse timings of the synthetic light curves obtained from our spot models to be compatible with the TESS ETV of the system. In this context, we calculated the primary and secondary eclipse timings of the model light curves cycle by cycle for

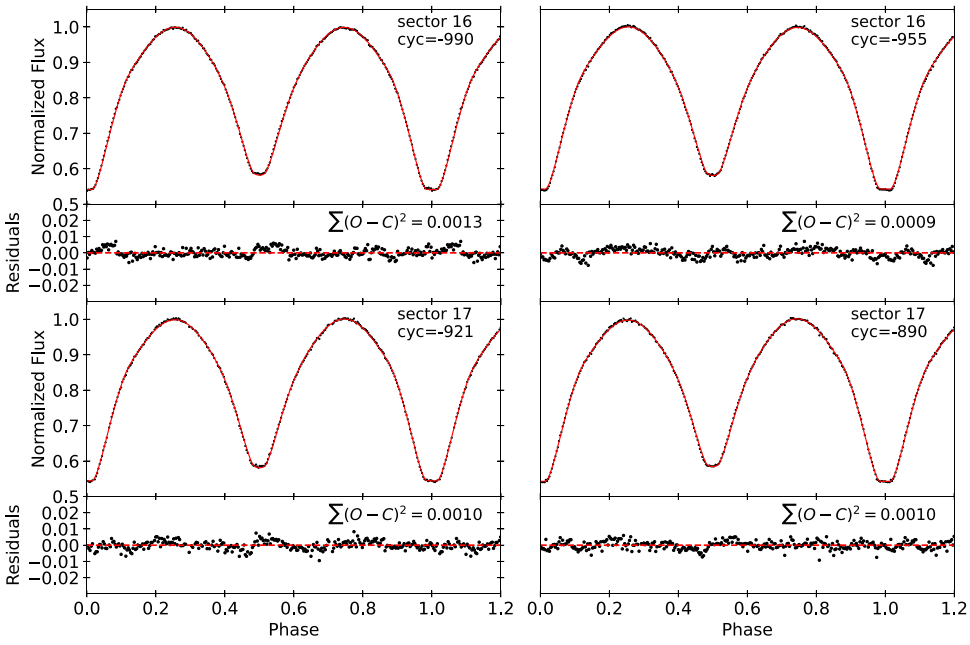


Fig. 8. Same as Figure Fig. 6 but for overlapping two-spots approximation.

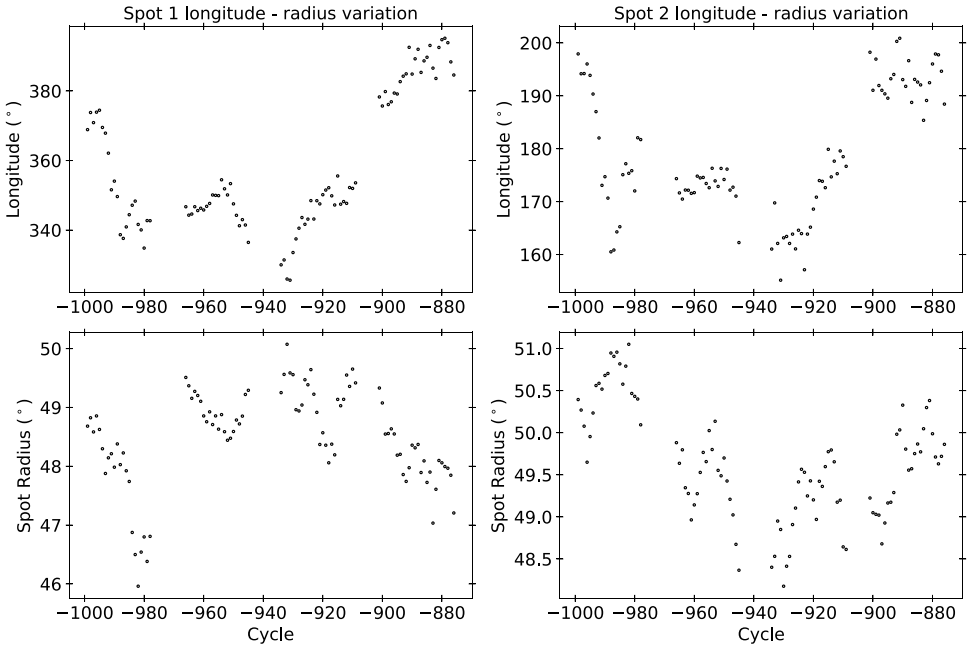


Fig. 9. Variation of spot longitudes and radii obtained from overlapping two-spots approximation. Note that some of the longitude values for spot 1 are plotted higher than 360° for better tracing of variation.

three different spot approximations mentioned in Section 4. We again ran the software `Xtrema` (Bahar et al., 2015) to calculate the synthetic primary and secondary eclipse timings. The comparison of TESS ETVs and the synthetic ETV diagrams obtained using the eclipse timings of model light curves for all spot approximations are plotted in Fig. 12.

From the top panel of Fig. 12, which shows a comparison of ETVs calculated from the TESS data and the single spot approximation, it is clear that the synthetic ETV cannot fully represent the observed ETV nature of the system, although the anti-correlated nature has emerged. The linear trend of the synthetic ETV diagram is also clearly noticeable. The mid and bottom panels, that compare the observed ETV with the ETVs of overlapping and non-overlapping two-spots configurations, appear to be compatible with the observed one, as they are able to represent both the anti-correlation and the quadratic trend. Therefore, in the case of the PP Lac system, the presence of two spots that are centred 180° apart from each other is the most plausible model that explains both the light curve asymmetries and the ETV behaviour.

6. The overall ETV behaviour

As mentioned in Section 1, the most recent ETV study of PP Lac was carried out by Kjurkchieva et al. (2020), who noticed episodic variation with a constant period that is superimposed on a cyclic behaviour. Therefore, in order to update the findings obtained by Kjurkchieva et al.

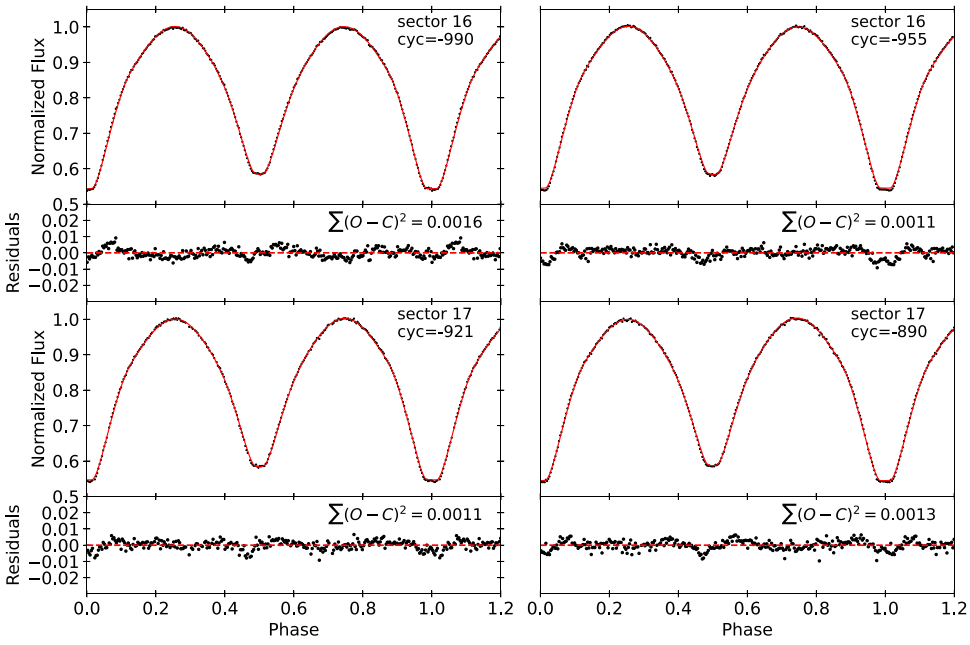


Fig. 10. Same as Fig. 6 but for non-overlapping two-spots approximation.

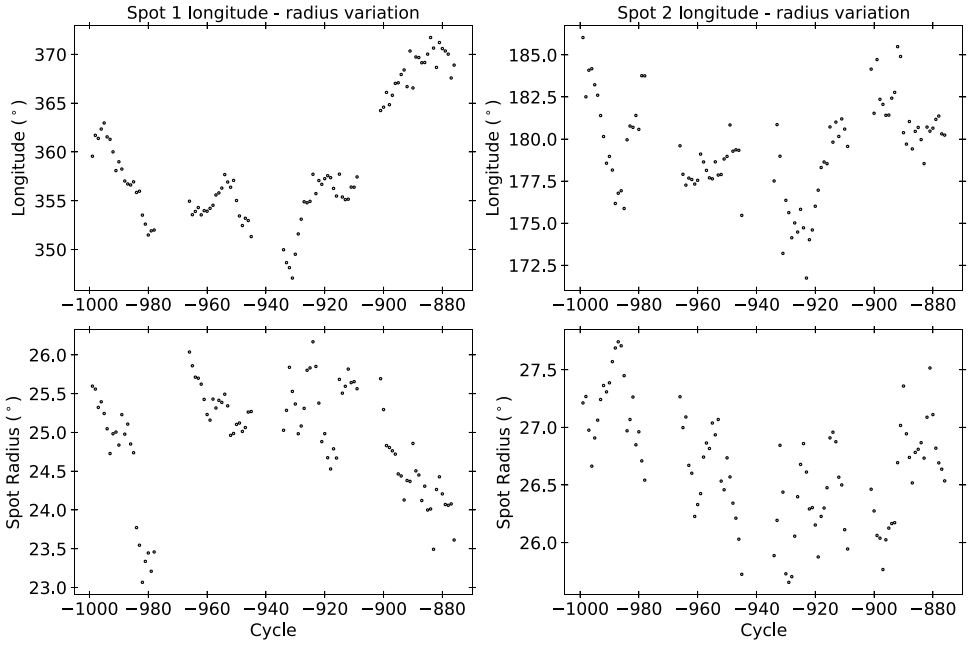


Fig. 11. Same as Fig. 9 but for non-overlapping two-spots approximation.

Table 3
Mid-eclipse times of PP Lac obtained in this study.

Time of Min. (Error) HJD2400000+	Type of Min.	Telescope/Filter
59139.44226(4)	I	T80/g', r', i'
59139.24196(3)	II	T80/g', r', i'
59711.50462(10)	I	OAUJ-CDK500/I, Sy

(2020), we also examined the overall ETV behaviour of PP Lac using all the available data in the literature, as well as the 3 mid-eclipse times obtained in this study that are listed in Table 3.

The current mid-eclipse times include 161 visual, 4 photographic, 7 photoelectric, 100 CCD and 191 TESS CCD data that spread over the years 1976 till 2022, covering ~41560 orbital cycles of the system. Since the visual mid-eclipse times are highly scattered compared to the overall variation, we considered seasonal averages and hence obtained 15 mean and 5 individual visual mid-eclipse times as the input data for the analysis. The entire mid-eclipse times were converted to the same time scale, as BJD. The ETV analysis of the system were carried out with the help of an IDL[6] code that is improved by our working group that was used during the ETV analyses of several eclipsing binaries in the literature performed by Özavcı et al. (2020), Yılmaz et al. (2017), Zola et al. (2016), Baştürk et al. (2015) and Zola et al. (2012). Based on the Levenberg–Marquardt algorithm (Markwardt, 2009), the

[6] https://www.l3harrisgeospatial.com/Software-Technology/IDL

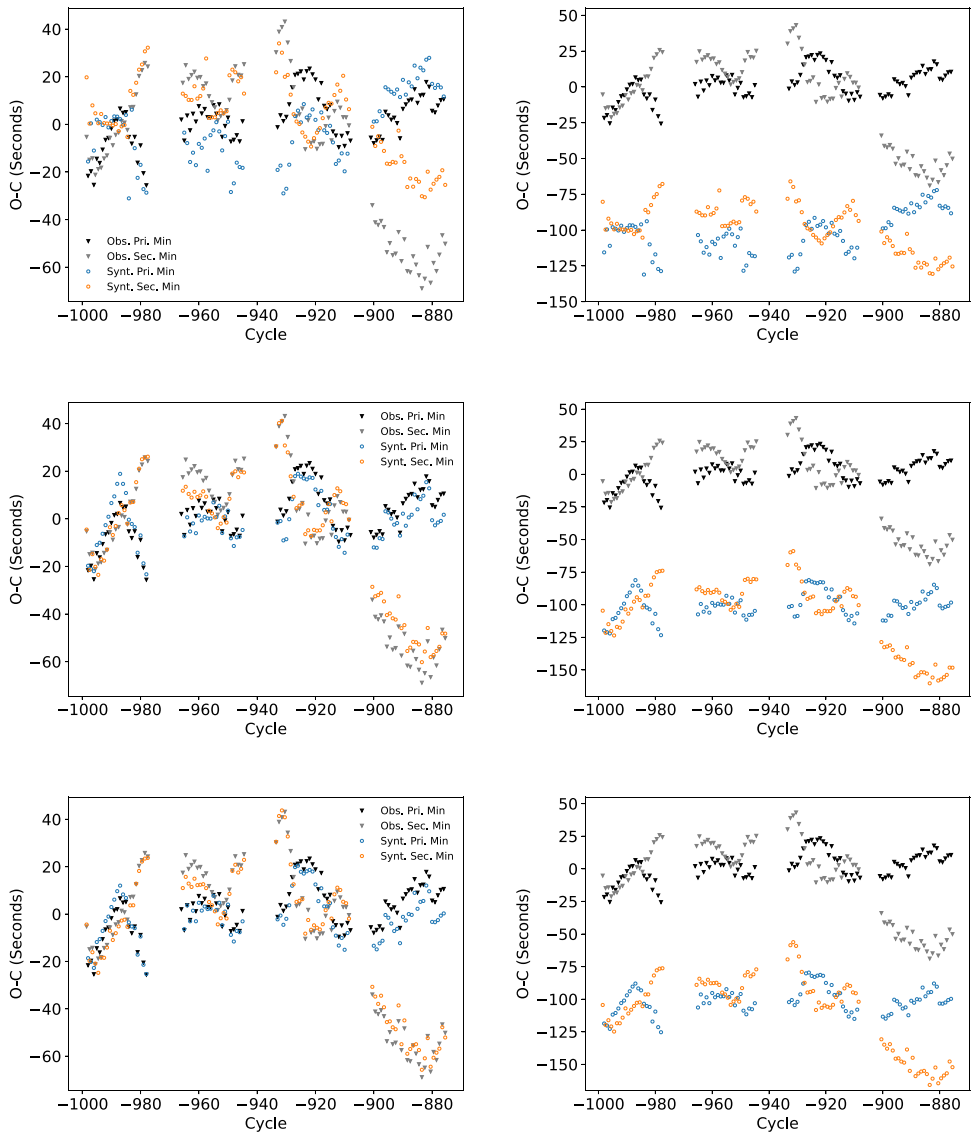


Fig. 12. The comparison of TESS ETVs with synthetic ETV diagrams for three spot approximations considered. Black and grey triangles show primary and secondary eclipse timings calculated from the TESS data, while the blue and orange open circles represent the same but for the eclipse timings obtained using the synthetic light curves. In the right column, ETVs are shifted vertically (~100 s) by different amounts for better visualization. Top, mid and bottom panels represent the ETV diagrams for single spot, overlapping two-spots and non-overlapping two-spots configurations, respectively.

code enables us to model the ETV behaviour of eclipsing binaries, considering all the well-known mechanisms in the literature such as mass transfer, light-time effect, magnetic activity and apsidal motion. The code uses Irwin's (1952) equations to derive the orbital parameters of additional bodies (light-time effect), while the Applegate (1992) formalism is used for the determination of magnetic activity related parameters. During the analysis, the weight values were adopted as 10 for CCD and TESS data, 8 for photoelectric and 1 for visuals and photographics. Depending on the previous studies as well as the most recent ETV diagram of PP Lac, we started the analysis by modelling two cyclic variations and a linear correction, among which the cyclic behaviours were assumed as light-time effect (LiTE) due to the presence of additional bodies. However, we could not obtain convincing model fits, as the residuals show a quadratic trend. Therefore, as a second trial, we assumed two cyclic (LiTE) variations superimposed on a quadratic change, which resulted in a satisfactory modelling of the data, as shown in Fig. 13. The obtained parameters are listed in the second column of Table 4.

In order to check if the orbital configurations for two LiTE assumption (hereafter Model-1) are stable, we performed orbital stability simulations using the `Rebound` N-body integrator package improved by Rein and Liu (2012) and the adaptive time stepping IAS15 integrator by Rein and Spiegel (2015). During the simulations, we assumed the additional bodies to have co-planar orbits with the binary. Using the parameters obtained from Model-1, we investigated the variations of the semi-major axis and eccentricity parameters of the third and fourth bodies, considering an integration time of 10000 years. The simulations showed that such a configuration becomes unstable in less than one orbital cycle of the inner body, as two bodies are very close to each other around the inner conjunction. Consequently, from the orbital stability test results, we can interpret that the current ETV behaviour cannot be represented by the existence of two additional bodies physically bound to the PP Lac system. On the other hand, both the light curves and the TESS ETV of the system clearly indicate the presence of spot(s) on one or both components. Assuming the cooler component is the active one, we performed two more trials based on the formalism of Applegate (1992) and considering one of the cyclic periods is due to the magnetic activity of the secondary component. In this context, as Model-2, we assume the longer period as magnetic activity cycle and the shorter one as LiTE, while in Model-3 we take into account the

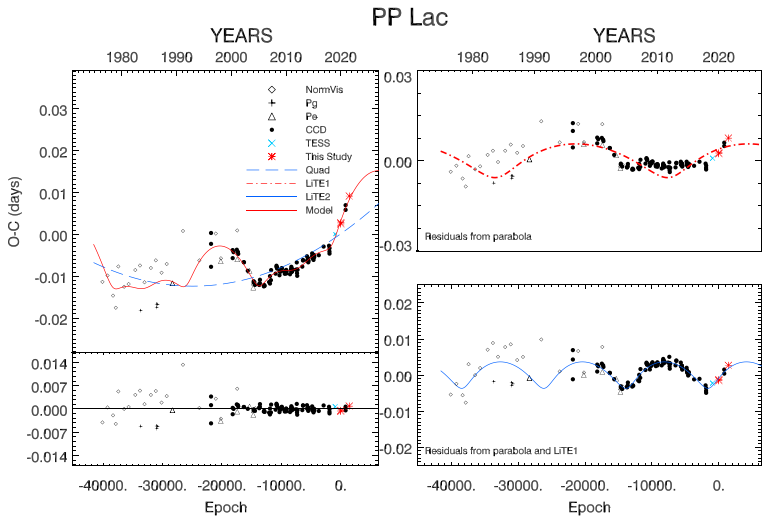


Fig. 13. ETV diagram and the model fits for two LiTE and a quadratic change assumption (Model-1). Description of the each subplots as well as the symbols are given in the figure.

Table 4
Best-fit parameters obtained from the overall ETV analysis of PP Lac. The second column includes the results from two LiTE assumption. The third column shows the results of the analysis that we attribute the long-term variation to magnetic activity and the short-term one to LiTE, while the fourth column lists the parameters from the opposite approach.

Parameter	Model-1	Model-2	Model-3
dM/dt [$M_\odot yr^{-1}$]	3.53(43)×10^{-8}	3.30(08)×10^{-9}	4.10(10)×10^{-8}
dP/dt [days yr^{-1}]	3.67(44)×10^{-8}	3.44(51)×10^{-9}	4.28(70)×10^{-8}
$T_{0,3}$ [HJD]	2451645(412)	–	2451509(513)
$P_3 LiTE$ [yr]	28.37(58)	–	29.28(62)
$A_3 LiTE$ [days]	0.0056(3)	–	0.0062(3)
e_3	0.44(9)	–	0.56(3)
w_3 [°]	284(4)	–	272(8)
$a_{12}\sin i_{12}$ [AU]	0.98(18)	–	1.08(10)
$f(M_3)[M_\odot]$	0.0012(7)	–	0.0015(4)
$M_3[M_\odot]$	0.189(2)	–	0.205(2)
$T_{0,4}$[HJD]	2444940(307)	–	–
$P_4 LiTE$ [yr]	13.48(22)	13.81(28)	–
$A_4 LiTE$ [days]	0.0037(2)	0.0023(2)	–
e_4	0.45(14)	0.65(13)	–
w_4 [°]	283(17)	339(10)	–
$a_{123}\sin i_{123}$ [AU]	0.64(14)	0.50(12)	–
$f(M_4)[M_\odot]$	0.0014(10)	0.0006(1)	–
$M_4[M_\odot]$	0.214(2)	0.162(7)	–
P_{Mag} [yr]	–	29.33(62)	13.63(22)
A_{Mag} [days]	–	0.0056(2)	0.0039(2)
B [Gauss]	–	6228(334)	11117(651)
ΔL [$L_\odot$]	–	0.028(4)	0.134(24)
Δm [mags]	–	0.010(2)	0.046(8)
$\Delta P/P$ (×10^{-6})	–	3.31(14)	4.90(32)
ΔE [erg]	–	3.20(49)×10^{40}	7.02(27)×10^{40}
ΔJ [g cm^2 s^{-1}]	–	1.76(13)×10^{47}	2.61(23)×10^{47}

dM/dt ($M_\odot yr^{-1}$): mass transfer rate, dP/dt (days yr^{-1}): period change rate, $P_3 LiTE$ (yr): orbital period of the third body, $A_3 LiTE$ (days): semi-amplitude generated by the presence of third body, e_3: orbital eccentricity of the third body, w_3 (°): the periastron angle of the third body orbit, $a_{12}\sin i_{12}$ (au): projected distance between the mass centre of the triple system and the eclipsing pair, f(M_3)($M_\odot$): mass function of the third body, $M_3(M_\odot)$: the mass of the third body, $P_4 LiTE$ (yr): orbital period of the fourth body, $A_4 LiTE$ (days): semi-amplitude generated by the presence of the fourth body, e_4: orbital eccentricity of the fourth body, w_4 (°): the periastron angle of the fourth body orbit, f(M_4)($M_\odot$): mass function of the fourth body, $M_4(M_\odot)$: mass of the fourth body, P_{Mag} [yr]: Period of the cyclic change under magnetic activity assumption, A_{Mag} [days]: semi-amplitude of the cyclic change under magnetic activity assumption, B[Gauss]: sub-surface magnetic field of the active (secondary) component, ΔL ($L_\odot$): the change of the luminosity of the secondary per activity cycle, Δm (mag): change of the brightness of the secondary per activity cycle, $\Delta P/P$: the relative variation of the orbital period, ΔE (erg): available energy for the secondary (active) component, ΔJ (g cm^{2}s^{-1}): the rate of angular momentum transfer.

opposite approximation (the longer period as LiTE and the shorter one as magnetic activity cycle). The best fit models for Model-2 and Model-3 are illustrated in Fig. 14 and Fig. 15, respectively, while the resultant parameters are listed in Table 4.

As presented in Table 4, we obtained the change of the luminosity of the secondary per activity cycle as ΔL=0.03$L_\odot$ and the corresponding change of the brightness as Δm=0.01 mag for Model-2, while the related parameters were calculated to be ΔL=0.13$L_\odot$ and Δm=0.05 mag, for Model-3. Since there is not enough photometric data of the system in the literature, we could not check the above given luminosity as well as the brightness changes and hence a reliable information about the magnetic activity cycle cannot be obtained. However, the modulation time scales as well as the relative variation of the orbital period ($\Delta P/P$), which are calculated of the order of $\sim 10^{-6}$ for both Model-2 and Model-3 are in accordance with the typical values for W UMa binaries that is mentioned by Lanza and Rodonò (1999). In order to further

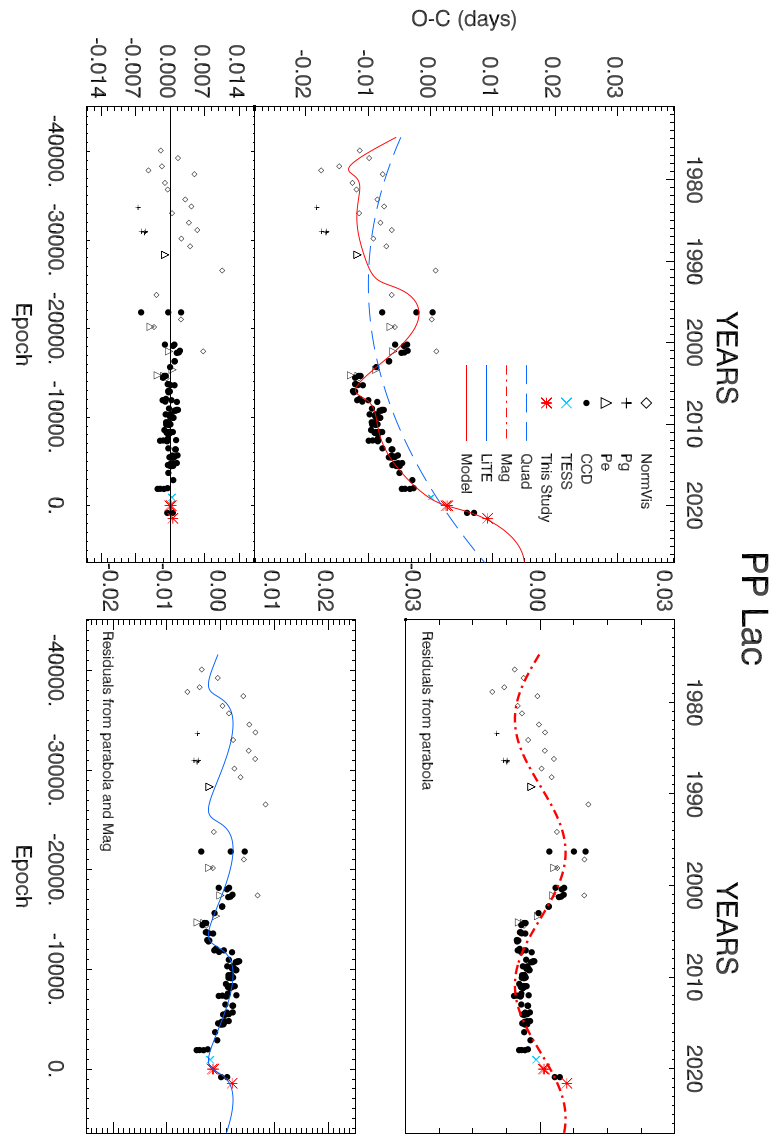


Fig. 14. Same as Fig. 13 but for Model-2.

strengthen the hypothesis that the cyclic variation is a consequence of magnetic activity as similarly performed by Hu et al. (2020), we calculated the energy required to drive the Applegate mechanism based on the formulations given by Brinkworth et al. (2006) and Völschow et al. (2016), by considering the variation of shell mass and hence the energy provided by the secondary component. The results are shown in Fig. 16, where both periodicities obtained for Model-2 and Model-3 ensure the required energies between $\sim$ 0.10–0.32 M_{shell}/M_{sec}. The results indicate that one of the cyclic variations seen on the current ETV behaviour of PP Lac system is most likely due to the magnetic activity of the secondary component, assuming both Model-2 and Model-3.

7. Conclusion and discussion

We carried out first simultaneous light and radial velocity curve analysis of the contact binary PP Lac using the ground-based SDSS g', r' and i' light curves obtained at the Ankara University Kreiken Observatory and the radial velocity data gathered at the Dominion Astrophysical Observatory. With the help of the absolute parameters from the simultaneous analysis as well as the high precision and continuous TESS data of the system, we investigate the spot activity under three different spot configurations as; single spot, overlapping two-spot and non-overlapping two-spot models. The ETV behaviour obtained using the TESS data of the system also enabled us a unique opportunity to check the consistencies of our spot models. The single spot model turned out to give unsatisfactory results for both light curve and ETV fits. On the other hand, the overlapping two-spots configuration resulted in convincing light curve model fits and ETVs. In fact, as we know from the solar spots and several Doppler imaging of active stars, the stellar spots are not exactly circular. Thus, the non-circular spot morphology could essentially be simulated by the overlapping two-spots approach assumed in this study. Besides, the overlapping spots were also recovered for the giant XX Tri by Künstler et al. (2015) using the Doppler imaging technique. Ascending and descending longitudinal drift of spots that are ~180° apart from each other on average is another remarkable point, as such longitudinal drifts are also present in the Doppler images of XX Tri and nicely demonstrated with an animation.[7] The non-overlapping two-spots configuration, where the spots located at high latitudes with the longitudinal distributions separated by ~180° on average, gave very similar results to those obtained in the overlapping two-spots approach.

[7] https://youtu.be/Zhi7ETLPExM

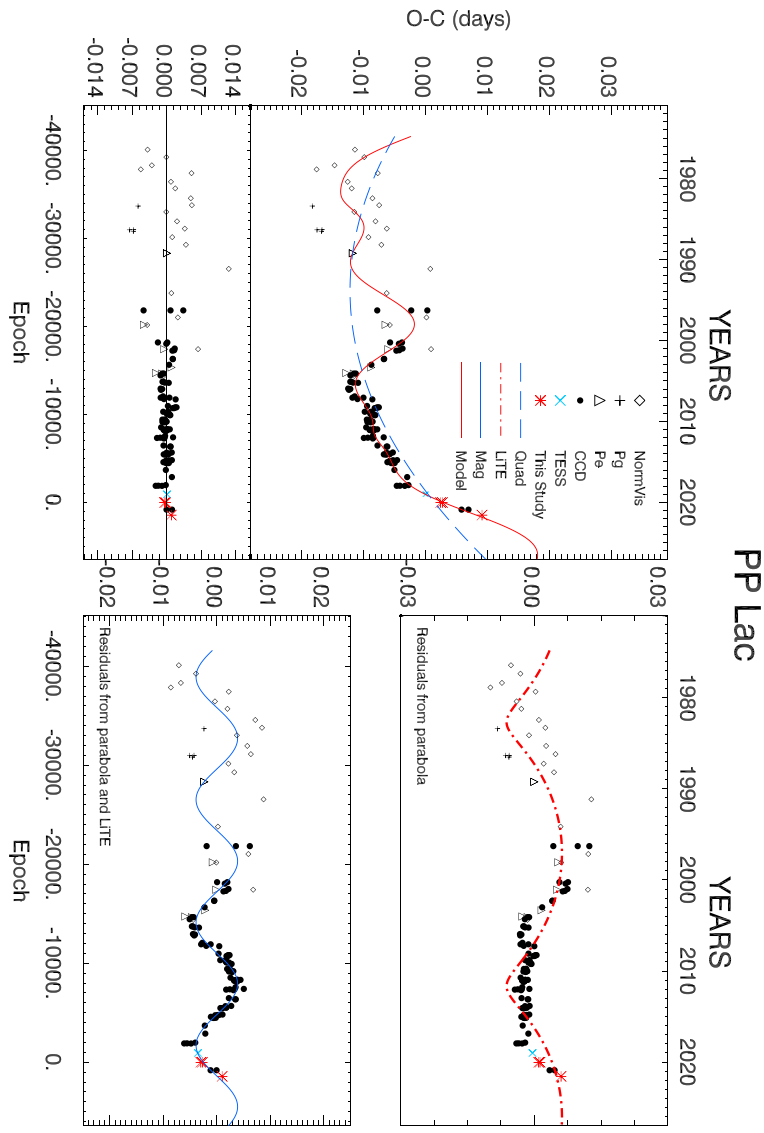


Fig. 15. Same as Fig. 13 but for Model-3.

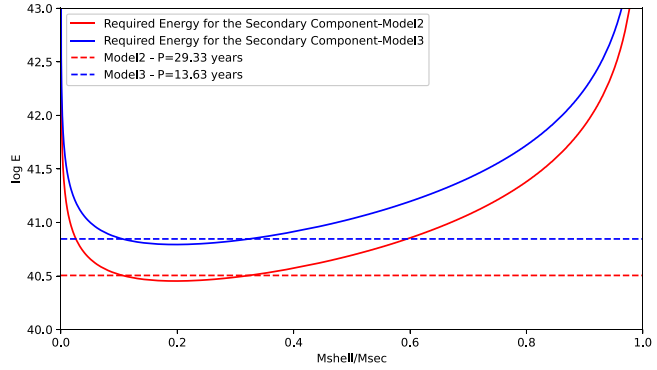


Fig. 16. Required energies for the secondary component for Model-2 (blue solid line) and Model-3 (red solid line) to drive Applegate mechanism as a function of the ratio of shell mass and total mass. The blue and red dotted lines represent the energy produced in the secondary component for Model-2 and Model-3, respectively.

The active or preferred longitudes, where spots preferably occur, is a well-known phenomena seen among the active single and binary stars (see Berdyugina, 2005 for details). Oláh et al. (2002) pointed out that the preferred longitudes in binary stars exist commonly at the sub-stellar points, which coincides with our results, as the spots drift around longitudes 180° and 360°. In addition, Holzwarth and Schüssler (2002) suggested a longitudinal dependence as a consequence of tidal effects in binary stars, which is dominant in the case of contact binaries. As a result, both the overlapping and non-overlapping two-spots models considered in this study are in agreement with the findings in the literature.

The anti-correlated behaviour seen in the Kepler and TESS ETV diagrams of binary stars was explained by the presence of a starspot that moves in longitude in the rotating frame of the binary, after Tran et al. (2013), who found ∼ 390 short-period binaries having such ETV nature and by Balaji et al. (2015), who suggested new method for tracking the phases of the orbital modulations in order to follow starspots. On the other hand, both studies consider single spot model and the systems having low orbital inclination. In the case of PP Lac, we have very high orbital inclination (i ∼ 84°) and most probably two spot regions. Therefore, we searched for a relation between the longitudinal variation of spots and observed TESS ETVs of PP Lac. Although we plotted the variations of spot longitudes and radii individually for two-spots approximations in Section 4, this time, we evaluated the longitude and radius variations of both spots together, as shown in Fig. 17.

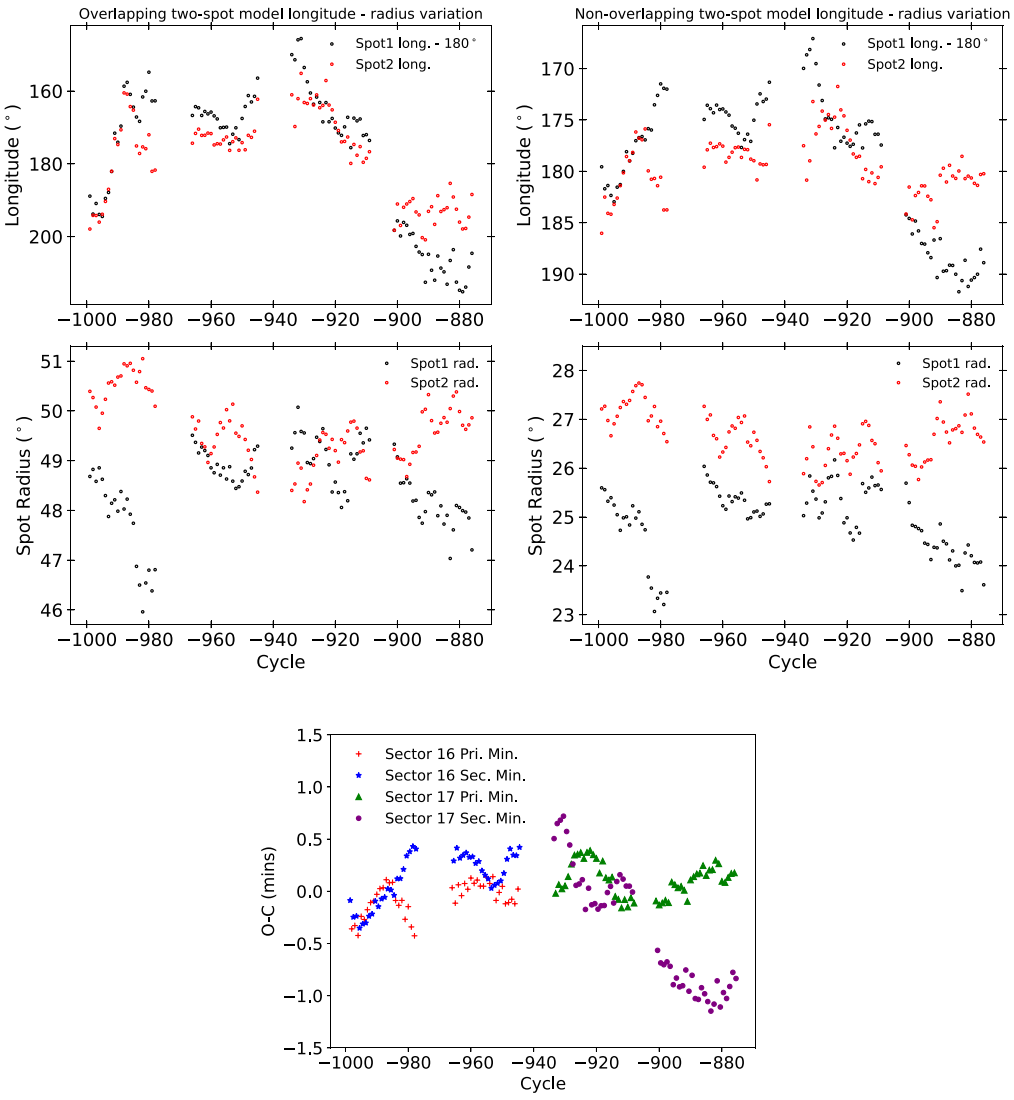


Fig. 17. Longitude-radius variations of overlapping (left panel) and non-overlapping (right panel) two-spot models. The bottom panel shows the TESS ETV diagram of PP Lac, for comparison. Note that the longitude axis is reversed (running from high to low).

Since there is ∼ 180° longitudinal separation between two spots, we subtracted 180° from the longitude of the first spot for a better comparison. The top panel of Fig. 17 shows the longitudinal variation of two spots for both overlapping (left panel) and non-overlapping (right panel) two-spots approximations. It should be noted that longitude axis is reversed (running from high to low) to better compare to the ETV diagram. The comparison of longitudinal variation and the ETV diagram clearly shows a correlation in both the anti-correlated behaviour and the quadratic trend. It can also be seen from this figure that spot No. 1 affects the secondary eclipse timings, while spot No. 2 affects the primary ones. It is an expected result, since spot No. 1 dominates the longitude 360° of the secondary component, which corresponds to the line of sight during the secondary eclipse. This is almost the same for spot No. 2, but for the primary eclipse. Another striking result is the deviation of eclipse timings from zero point (0 min), as the spots drift away from ∼ 180° and ∼ 360° longitudes with the maximum separations of ±30° and ±10° for overlapping and non-overlapping two-spot models, respectively. In addition, the variation in the radii of the spots also shows an anti-correlated structure, being in the order of ±2° for both spots. In order to inspect the effect of slight variation of spot radii on the light curve solution and the ETV, we performed another run for overlapping two-spot model by keeping the average radii of spots fixed and only adjusting the longitudes. The results turned out to show discrepancies in both model light curves and ETV, being substantially higher for the former one. Thus, although the amount is small, it was revealed that the variation of spot radii significantly affects both the light curve and the ETV.

The overall findings indicate that the light variation without eclipses as well as the ETV nature seen in the TESS light curves of the contact binary PP Lac can be explained most likely by the presence of two high latitude or polar spot groups, whose longitudes and radii show quasi-periodic variations. In addition, the high latitude spots of PP Lac are also consistent with the results obtained by Tran et al. (2013), who emphasized that the high inclination angles require starspots to be located close to the poles of the components to produce anti-correlated ETV curves. Therefore, the obtained results clearly show that the ETV behaviour of the system must be considered in order to obtain realistic spot parameters from the light curve analysis. The overlapping two-spot model may actually be a counterpart of a non-circular polar spot structure or a single spot with umbra and penumbra. Moreover, the Doppler images of contact binary stars showed that the spots may be distributed on both components (i.e. Barnes et al., 2004, Şenavcı et al., 2011), while it is not possible to obtain such information only using photometry. In this context, combining the information from ETVs of contact binaries with robust techniques such as Doppler imaging can provide us further clues on the activity behaviour of such systems,

which is not yet fully understood. The orbital stability tests as well as the Applegate theory-based analysis results indicate that the two periodicities seen on the overall ETV diagram of PP Lac may be a combination of both the LiTE and magnetic activity mechanisms and will become more clear when further eclipse timings data are obtained.

Declaration of competing interest

The authors declare that they have no known competing financial interests or personal relationships that could have appeared to influence the work reported in this paper.

Data availability

Data will be made available on request.

Acknowledgements

This paper is dedicated to the memory of Robert Howard Nelson, who passed away on November 1st, 2022. This work is supported by the research fund of Ankara University (BAP) through the project 18A0759001. The authors acknowledge the use of the Simbad database (http://simbad.u-strasbg.fr/simbad/), operated at the CDS, Strasbourg, France, and NASA's Astrophysics Data System Bibliographic Services (http://adsabs.harvard.edu/). Funding for the TESS mission is provided by NASA's Science Mission directorate.

References

Al-Naimiy, H.M.K., Al-Hindawy, A.M.A., 1992. A new set of geometrical and physical elements of the eclipsing variable Pp-lacertae. Astrophys. Space Sci. 198 (2), 231–236. http://dx.doi.org/10.1007/BF00644755.

Applegate, J.H., 1992. A mechanism for orbital period modulation in close binaries. Astrophys. J. 385, 621. http://dx.doi.org/10.1086/170967.

Baştürk, Ö., Zola, S., Liakos, A., Nelson, R.H., Gazeas, K., Özavcı, İ., Yılmaz, M., Şenavcı, H.V., Zakrzewski, B., 2015. The absolute parameters of the detached eclipsing binary V482 Per. New Astron. 41, 42–47. http://dx.doi.org/10.1016/j.newast.2015.04.008, arXiv:1508.06114.

Bahar, E., Šenavcı, H.V., Baştürk, Ö., 2015. A python-based GUI software to calculate times of maximum and minimum: Xtrema. In: Rucinski, S.M., Torres, G., Zejda, M. (Eds.), Living Together: Planets, Host Stars and Binaries. In: Astronomical Society of the Pacific Conference Series, vol. 496, p. 288.

Balaji, B., Croll, B., Levine, A.M., Rappaport, S., 2015. Tracking the stellar longitudes of starspots in short-period Kepler binaries. Mon. Not. R. Astron. Soc. 448 (1), 429–444. http://dx.doi.org/10.1093/mnras/stv031, arXiv:1412.8101.

Barnes, J.R., Lister, T.A., Hilditch, R.W., Collier Cameron, A., 2004. High-resolution Doppler images of the spotted contact binary AE Phe. Mon. Not. R. Astron. Soc. 348 (4), 1321–1331. http://dx.doi.org/10.1111/j.1365-2966.2004.07452.x.

Berdyugina, S.V., 2005. Starspots: A key to the stellar dynamo. Living Rev. Sol. Phys. 2 (1), 8. http://dx.doi.org/10.12942/lrsp-2005-8.

Brasseur, C.E., Phillip, C., Fleming, S.W., Mullally, S.E., White, R.L., 2019. Astrocut: Tools for creating cutouts of TESS images. arXiv:1905.007.

Brinkworth, C.S., Marsh, T.R., Dhillon, V.S., Knigge, C., 2006. Detection of a period decrease in NN ser with ULTRACAM: evidence for strong magnetic braking or an unseen companion. Mon. Not. R. Astron. Soc. 365 (1), 287–295. http://dx.doi.org/10.1111/j.1365-2966.2005.09718.x, arXiv:astro-ph/0510331.

Collins, K.A., Kielkopf, J.F., Stassun, K.G., Hessman, F.V., 2017. AstroImageJ: Image processing and photometric extraction for ultra-precise astronomical light curves. Astron. J. 153 (2), 77. http://dx.doi.org/10.3847/1538-3881/153/2/77, arXiv:1701.04817.

Dumont, M., Maraziti, A., 1990. First BV light curve for the eclipsing binary PP lacertae. Inf. Bull. Var. Stars 3478, 1.

Figer, A., Rolland, R., 1977. NN cephei and PP lacertae. Inf. Bull. Var. Stars 1231, 1.

Gaia Collaboration, Mignard, F., Klioner, S.A., Lindegren, L., Hernández, J., Bastian, U., Bombrun, A., Hobbs, D., Lammers, U., Michalik, D., Ramos-Lerate, M., Biermann, M., Fernández-Hernández, J., Geyer, R., Hilger, T., Siddiqui, H.I., Steidelmüller, H., Babusiaux, C., Barache, C., Lambert, S., Andrei, A.H., Bourda, G., Charlot, P., Brown, A.G.A., Vallenari, A., Prusti, T., de Bruijne, J.H.J., Bailer-Jones, C.A.L., Evans, D.W., Eyer, L., Jansen, F., Jordi, C., Luri, X., Panem, C., Pourbaix, D., Randich, S., Sartoretti, P., Soubiran, C., van Leeuwen, F., Walton, N.A., Arenou, F., Cropper, M., Drimmel, R., Katz, D., Lattanzi, M.G., Bakker, J., Cacciari, C., Castañeda, J., Chaoul, L., Cheek, N., De Angeli, F., Fabricius, C., Guerra, R., Holl, B., Masana, E., Messineo, R., Mowlavi, N., Nienartowicz, K., Panuzzo, P., Portell, J., Riello, M., Seabroke, G.M., Tanga, P., Thévenin, F., Gracia-Abril, G., Comoretto, G., Garcia-Reinaldos, M., Teyssier, D., Altmann, M., Andrae, R., Audard, M., Bellas-Velidis, I., Benson, K., Berthier, J., Blomme, R., Burgess, P., Busso, G., Carry, B., Cellino, A., Clementini, G., Clotet, M., Creevey, O., Davidson, M., De Ridder, J., Delchambre, L., Dell'Oro, A., Ducourant, C., Fouesneau, M., Frémat, Y., Galluccio, L., García-Torres, M., González-Núñez, J., González-Vidal, J.J., Gosset, E., Guy, L.P., Halbwachs, J.L., Hambly, N.C., Harrison, D.L., Hestroffer, D., Hodgkin, S.T., Hutton, A., Jasniewicz, G., Jean-Antoine-Piccolo, A., Jordan, S., Korn, A.J., Krone-Martins, A., Lanzafame, A.C., Lebzelter, T., Löffler, W., Manteiga, M., Marrese, P.M., Martín-Fleitas, J.M., Moitinho, A., Mora, A., Muinonen, K., Osinde, J., Pancino, E., Pauwels, T., Petit, J.M., Recio-Blanco, A., Richards, P.J., Rimoldini, L., Robin, A.C., Sarro, L.M., Siopis, C., Smith, M., Sozzetti, A., Süveges, M., Torra, J., van Reeven, W., Abbas, U., Abreu Aramburu, A., Accart, S., Aerts, C., Altavilla, G., Álvarez, M.A., Alvarez, R., Alves, J., Anderson, R.I., Anglada Varela, E., Antiche, E., Antoja, T., Arcay, B., Astraatmadja, T.L., Bach, N., Baker, S.G., Balaguer-Núñez, L., Balm, P., Barata, C., Barbato, D., Barblan, F., Barklem, P.S., Barrado, D., Barros, M., Barstow, M.A., Bartholomé Muñoz, L., Bassilana, J.L., Becciani, U., Bellazzini, M., Berihuete, A., Bertone, S., Bianchi, L., Bienaymé, O., Blanco-Cuaresma, S., Boch, T., Boeche, C., Borrachero, R., Bossini, D., Bouquillon, S., Bragaglia, A., Bramante, L., Breddels, M.A., Bressan, A., Brouillet, N., Brüsemeister, T., Brugaletta, E., Bucciarelli, B., Burlacu, A., Busonero, D., Butkevich, A.G., Buzzi, R., Caffau, E., Cancelliere, R., Cannizzaro, G., Cantat-Gaudin, T., Carballo, R., Carlucci, T., Carrasco, J.M., Casamiquela, L., Castellani, M., Castro-Ginard, A., Chemin, L., Chiavassa, A., Cocozza, G., Costigan, G., Cowell, S., Crifo, F., Crosta, M., Crowley, C., Cuypers, J., Dafonte, C., Damerdji, Y., Dapergolas, A., David, P., David, M., de Laverny, P., De Luise, F., De March, R., de Souza, R., de Torres, A., Debosscher, J., del Pozo, E., Delbo, M., Delgado, A., Delgado, H.E., Diakite, S., Diener, C., Distefano, E., Dolding, C., Drazinos, P., Durán, J., Edvardsson, B., Enke, H., Eriksson, K., Esquej, P., Eynard Bontemps, G., Fabre, C., Fabrizio, M., Faigler, S., Falcão, A.J., Farràs Casas, M., Federici, L., Fedorets, G., Fernique, P., Figueras, F., Filippi, F., Findeisen, K., Fonti, A., Fraile, E., Fraser, M., Frézouls, B., Gai, M., Galleti, S., Garabato, D., García-Sedano, F., Garofalo, A., Garralda, N., Gavel, A., Gavras, P., Gerssen, J., Giacobbe, P., Gilmore, G., Girona, S., Giuffrida, G., Glass, F., Gomes, M., Granvik, M., Gueguen, A., Guerrier, A., Guiraud, J., Gutié, R., Haigron, R., Hatzidimitriou, D., Hauser, M., Haywood, M., Heiter, U., Helmi, A., Heu, J., Hofmann, W., Holland, G., Huckle, H.E., Hypki, A., Icardi, V., Janßen, K., Jevardat de Fombelle, G., Jonker, P.G., Juhász, A.L., Julbe, F., Karampelas, A., Kewley, A., Klar, J., Kochoska, A., Kohley, R., Kolenberg, K., Kontizas, M., Kontizas, E., Koposov, S.E., Kordopatis, G., Kostrzewa-Rutkowska, Z., Koubsky, P., Lanza, A.F., Lasne, Y., Lavigne, J.B., Le Fustec, Y., Le Poncin-Lafitte, C., Lebreton, Y., Leccia, S., Leclerc, N., Lecoeur-Taibi, I., Lenhardt, H., Leroux, F., Liao, S., Licata, E., Lindstrøm, H.E.P., Lister, T.A., Livanou, E., Lobel, A., López, M., Managau, S., Mann, R.G., Mantelet, G., Marchal, O., Marchant, J.M., Marconi, M., Marinoni, S., Marschalkó, G., Marshall, D.J., Martino, M., Marton, G., Mary, N., Massari, D., Matijevič, G., Mazeh, T., McMillan, P.J., Messina, S., Millar, N.R., Molina, D., Molinaro, R., Molnár, L., Montegriffo, P., Mor, R., Morbidelli, R., Morel, T., Morris, D., Mulone, A.F., Muraveva, T., Musella, I., Nelemans, G., Nicastro, L., Noval, L., O'Mullane, W., Ordénovic, C., Ordóñez-Blanco, D., Osborne, P., Pagani, C., Pagano, I., Pailler, F., Palacin, H., Palaversa, L., Panahi, A., Pawlak, M., Piersimoni, A.M., Pineau, F.X., Plachy, E., Plum, G., Poggio, E., Poujoulet, E., Prša, A., Pulone, L., Racero, E., Ragaini, S., Rambaux, N., Regibo, S., Reylé, C., Riclet, F., Ripepi, V., Riva, A., Rivard, A., Rixon, G., Roegiers, T., Roelens, M., Romero-Gómez, M., Rowell, N., Royer, F., Ruiz-Dern, L., Sadowski, G., Sagristà Sellés, T., Sahlmann, J., Salgado, J., Salguero, E., Sanna, N., Santana-Ros, T., Sarasso, M., Savietto, H., Schultheis, M., Sciacca, E., Segol, M., Segovia, J.C., Ségransan, D., Shih, I.C., Siltala, L., Silva, A.F., Smart, R.L., Smith, K.W., Solano, E., Solitro, F., Sordo, R., Soria Nieto, S., Souchay, J., Spagna, A., Spoto, F., Stampa, U., Steele, I.A., Stephenson, C.A., Stoev, H., Suess, F.F., Surdej, J., Szabados, L., Szegedi-Elek, E., Tapiador, D., Taris, F., Tauran, G., Taylor, M.B., Teixeira, R., Terrett, D., Teyssandier, P., Thuillot, W., Titarenko, A., Torra Clotet, F., Turon, C., Ulla, A., Utrilla, E., Uzzi, S., Vaillant, M., Valentini, G., Valette, V., van Elteren, A., Van Hemelryck, E., van Leeuwen, M., Vaschetto, M., Vecchiato, A., Veljanoski, J., Viala, Y., Vicente, D., Vogt, S., von Essen, C., Voss, H., Votruba, V., Voutsinas, S., Walmsley, G., Weiler, M., Wertz, O., Wevers, T., Wyrzykowski, Ł., Yoldas, A., Žerjal, M., Ziaeepour, H., Zorec, J., Zschocke, S., Zucker, S., Zurbach, C., Zwitter, T., 2018. Gaia data release 2. The celestial reference frame (Gaia-CRF2). Astron. Astrophys. 616, A14. http://dx.doi.org/10.1051/0004-6361/201832916, arXiv:1804.09377.

Gaspani, A., 1990. First synthetic solution for the W UMa system PP lac. Inf. Bull. Var. Stars 3534, 1.

Güzel, O., Özdarcan, O., 2020. PyWD2015 - A new GUI for the Wilson-Devinney code. In: Contributions of the Astronomical Observatory Skalnate Pleso. Vol. 50. No. 2. pp. 535–538. http://dx.doi.org/10.31577/caosp.2020.50.2.535.

Hendry, P.D., Mochnacki, S.W., 2000. Doppler imaging of VW cephei: Distribution and evolution of starspots on a contact binary. Astrophys. J. 531 (1), 467–493. http://dx.doi.org/10.1086/308427.

Holzwarth, V., Schüssler, M., 2002. Do tidal effects determine the spot distribution on active binaries? Astron. Nachr. 323, 399–401.

Hu, K., Yu, Y.-X., Zhang, J.-F., Xiang, F.-Y., 2020. Long-term photometry and orbital period change of the W UMa-type binary v0599 Aur: Evidence of about 11 yr magnetic-activity cycle. Astron. J. 160 (2), 62. http://dx.doi.org/10.3847/1538-3881/ab99c4.

Irwin, J.B., 1952. The determination of a light-time orbit. Astrophys. J. 116, 211. http://dx.doi.org/10.1086/145604.

Kasliwal, V.P., Vogeley, M.S., Richards, G.T., 2015. Are the variability properties of the Kepler AGN light curves consistent with a damped random walk? Mon. Not. R. Astron. Soc. 451, 4328–4345. http://dx.doi.org/10.1093/mnras/stv1230, arXiv:1505.00360.

Kjurkchieva, D.P., Popov, V.A., Petrov, N.I., 2020. Global parameters of the totally-eclipsing W UMa stars NSVS 6673994, NSVS 4316778, PP Lac and NSVS 1926064. New Astron. 77, 101352. http://dx.doi.org/10.1016/j.newast.2019.101352.

Künstler, A., Carroll, T.A., Strassmeier, K.G., 2015. Spot evolution on the red giant star XX Triangulum. A starspot-decay analysis based on time-series Doppler imaging. Astron. Astrophys. 578, A101. http://dx.doi.org/10.1051/0004-6361/201525687, arXiv:1504.02270.

Lanza, A.F., Rodonò, M., 1999. Orbital period modulation and quadrupole moment changes in magnetically active close binaries. Astron. Astrophys. 349, 887–897.

Lightkurve Collaboration, Cardoso, J.V.d.M., Hedges, C., Gully-Santiago, M., Saunders, N., Cody, A.M., Barclay, T., Hall, O., Sagear, S., Turtelboom, E., Zhang, J., Tzanidakis, A., Mighell, K., Coughlin, J., Bell, K., Berta-Thompson, Z., Williams, P., Dotson, J., Barentsen, G., 2018. Lightkurve: Kepler and TESS time series analysis in Python. arXiv:1812.013.

Lucy, L.B., 1967. Gravity-darkening for stars with convective envelopes. ZAP 65, 89.

Maehara, H., Notsu, Y., Notsu, S., Namekata, K., Honda, S., Ishii, T.T., Nogami, D., Shibata, K., 2017. Starspot activity and superflares on solar-type stars. Publ. Astron. Soc. Japan 69 (3), 41. http://dx.doi.org/10.1093/pasj/psx013, arXiv:1702.07141.

Markwardt, C.B., 2009. Non-linear least-squares fitting in IDL with MPFIT. In: Bohlender, D.A., Durand, D., Dowler, P. (Eds.), Astronomical Data Analysis Software and Systems XVIII. In: Astronomical Society of the Pacific Conference Series, vol. 411, p. 251, arXiv:0902.2850.

Maxted, P.F.L., Gaulme, P., Graczyk, D., Hełminiak, K.G., Johnston, C., Orosz, J.A., Prša, A., Southworth, J., Torres, G., Davies, G.R., Ball, W., Chaplin, W.J., 2020. The TESS light curve of AI phoenicis. Mon. Not. R. Astron. Soc. 498 (1), 332–343. http://dx.doi.org/10.1093/mnras/staa1662, arXiv:2003.09295.

Miller, W.J., Wachmann, A.A., 1971. VV281-427, variable stars in a cepheus-lacerta field of the milky way. Ricerche Astron. 8, 12.

Oláh, K., Strassmeier, K.G., Weber, M., 2002. Doppler imaging of stellar surface structure. XVIII. The very active RS CVn binary UZ Librae revisited. Astron. Astrophys. 389, 202–212. http://dx.doi.org/10.1051/0004-6361:20020506.

Özavcı, İ., Özuyar, D., Şenavcı, H.V., Yılmaz, M., Bahar, E., Baştürk, Ö., Kılıçoğlu, T., Elmaslı, A., Çalışkan, Ş., İzci, D.D., Yörükoğlu, O., Selam, S.O., 2020. Orbital period analysis of four eclipsing binaries XY Boo, RW Com, MR Del and AK Her. AcA 70 (1), 33–52. http://dx.doi.org/10.32023/0001-5237/70.1.3.

Qian, S.B., Zhu, L.Y., Boonruksar, S., 2005. The first CCD photometric study of the neglected W UMa-type binary PP Lacertae. New Astron. 11 (1), 52–58. http://dx.doi.org/10.1016/j.newast.2005.06.003.

Rein, H., Liu, S.F., 2012. REBOUND: an open-source multi-purpose N-body code for collisional dynamics. Astron. Astrophys. 537, A128. http://dx.doi.org/10.1051/0004-6361/201118085, arXiv:1110.4876.

Rein, H., Spiegel, D.S., 2015. IAS15: a fast, adaptive, high-order integrator for gravitational dynamics, accurate to machine precision over a billion orbits. Mon. Not. R. Astron. Soc. 446 (2), 1424–1437. http://dx.doi.org/10.1093/mnras/stu2164, arXiv:1409.4779.

Revalski, M., Nowak, D., Wiita, P.J., Wehrle, A.E., Unwin, S.C., 2014. Investigating the variability of active galactic nuclei using combined multi-quarter Kepler data. Astrophys. J. 785, 60. http://dx.doi.org/10.1088/0004-637X/785/1/60, arXiv:1311.4838.

Ruciński, S.M., 1969. The proximity effects in close binary systems. II. The bolometric reflection effect for stars with deep convective envelopes. AcA 19, 245.

Rucinski, S.M., 2004. Advantages of the broadening function (BF) over the cross-correlation function (CCF). In: Maeder, A., Eenens, P. (Eds.), Stellar Rotation. In: American Astronomical Society Meeting Abstracts, vol. 215, p. 17.

Sanders, S.J., Hargis, J.R., Bradstreet, D.H., 2004. New light curves and analysis of the overcontact binaries PP lac and DK sge. In: American Astronomical Society Meeting Abstracts. In: American Astronomical Society Meeting Abstracts, vol. 205, p. 18.08.

Schuessler, M., Solanki, S.K., 1992. Why rapid rotators have polar spots. Astron. Astrophys. 264, L13–L16.

Şenavcı, H.V., Hussain, G.A.J., O'Neal, D., Barnes, J.R., 2011. Investigating the surface inhomogeneities of the contact binary SW Lacertae. I. Doppler imaging. Astron. Astrophys. 529, A11. http://dx.doi.org/10.1051/0004-6361/201015753.

Tran, K., Levine, A., Rappaport, S., Borkovits, T., Csizmadia, S., Kalomeni, B., 2013. The anticorrelated nature of the primary and secondary eclipse timing variations for the Kepler contact binaries. Astrophys. J. 774 (1), 81. http://dx.doi.org/10.1088/0004-637X/774/1/81, arXiv:1305.4639.

van Hamme, W., 1993. New limb-darkening coefficients for modeling binary star light curves. Astron. J. 106, 2096. http://dx.doi.org/10.1086/116788.

Völschow, M., Schleicher, D.R.G., Perdelwitz, V., Banerjee, R., 2016. Eclipsing time variations in close binary systems: Planetary hypothesis vs. Applegate mechanism. Astron. Astrophys. 587, A34. http://dx.doi.org/10.1051/0004-6361/201527333, arXiv:1512.01960.

Wilson, R.E., Devinney, E.J., 1971. Realization of accurate close-binary light curves: Application to MR cygni. Astrophys. J. 166, 605. http://dx.doi.org/10.1086/150986.

Xiang, Y., Gu, S., Collier Cameron, A., Barnes, J.R., 2015. Doppler images of the eclipsing binary ER vulpeculae. Mon. Not. R. Astron. Soc. 447 (1), 567–576. http://dx.doi.org/10.1093/mnras/stu2458, arXiv:1411.5531.

Yang, Y., Wang, S., 2023. Chromospheric activity and period variations of the contact binary EE cet from TESS. New Astron. 98, 101919. http://dx.doi.org/10.1016/j.newast.2022.101919.

Yılmaz, M., Nelson, R.H., Şenavcı, H.V., İzci, D., Özavcı, İ., Gümüş, D., 2017. Light curve and orbital period analysis of VX lac. RMxAA 53, 29–36.

Zola, S., Baştürk, Ö., Liakos, A., Gazeas, K., Şenavcı, H.V., Nelson, R.H., Özavcı, İ., Zakrzewski, B., Yılmaz, M., 2016. Photometric, spectroscopic, and orbital period study of three early-type semi-detached systems: XZ aql, UX her, and AT peg. Astron. J. 152 (2), 33. http://dx.doi.org/10.3847/0004-6256/152/2/33, arXiv:1607.06930.

Zola, S., Nelson, R.H., Şenavcı, H.V., Szymanski, T., Kuźmicz, A., Winiarski, M., Jableka, D., 2012. Spectroscopic and photometric study of the contact binary BO CVn. New Astron. 17 (8), 673–678. http://dx.doi.org/10.1016/j.newast.2012.04.004, arXiv:1204.3584.